Observation of ultrahigh mobility surface states in a topological crystalline insulator by infrared spectroscopy

Ying Wang[1], Guoyu Luo[2], Junwei Liu[3,4], R. Sankar[5,6], Nan-Lin Wang[7], Fangcheng Chou[5], Liang Fu[3] & Zhiqiang Li[2]

Topological crystalline insulators possess metallic surface states protected by crystalline symmetry, which are a versatile platform for exploring topological phenomena and potential applications. However, progress in this field has been hindered by the challenge to probe optical and transport properties of the surface states owing to the presence of bulk carriers. Here, we report infrared reflectance measurements of a topological crystalline insulator, (001)-oriented $Pb_{1-x}Sn_xSe$ in zero and high magnetic fields. We demonstrate that the far-infrared conductivity is unexpectedly dominated by the surface states as a result of their unique band structure and the consequent small infrared penetration depth. Moreover, our experiments yield a surface mobility of $40,000\,cm^2\,V^{-1}\,s^{-1}$, which is one of the highest reported values in topological materials, suggesting the viability of surface-dominated conduction in thin topological crystalline insulator crystals. These findings pave the way for exploring many exotic transport and optical phenomena and applications predicted for topological crystalline insulators.

[1] National High Magnetic Field Laboratory, Tallahassee, FL 32310, USA. [2] College of Physical Science and Technology, Sichuan University, Chengdu, Sichuan 610064, China. [3] Department of Physics, Massachusetts Institute of Technology, Cambridge, MA 02139, USA. [4] Department of Physics, Hong Kong University of Science and Technology, Clear Water Bay, Hong Kong, China. [5] Center for Condensed Matter Sciences, National Taiwan University, Taipei 10617, Taiwan. [6] Institute of Physics, Academia Sinica, Taipei 11529, Taiwan. [7] International Center for Quantum Materials, School of Physics, Peking University, Beijing 100871, China. Correspondence and requests for materials should be addressed to Z.L. (email: zhiqiangli@scu.edu.cn)

Recently, a new class of insulators called topological crystalline insulators (TCIs) were predicted and observed in IV–VI semiconductors[1–8], which have attracted tremendous scientific interest[8–17]. These materials host gapless Dirac-like surface states (SS) that are protected by crystalline symmetry[1, 2] instead of time-reversal symmetry[18–20]. Consequently, breaking the crystal symmetry can open a band gap in these SS[3, 12], offering new opportunities for band gap engineering by strain or structural distortion. Moreover, compared with Z_2 topological insulators[18–20], the (001) SS of TCIs have been predicted to exhibit a wider range of tunable electronic properties under many types of perturbations breaking the crystalline symmetry, such as interface superconductivity[9], spin-filtered edge states[10], quantum anomalous Hall effect[11], Weyl fermions[13], and valley-dependent optical properties[14]. Therefore, TCIs are emerging as a very versatile material system not only for exploring topological quantum phenomena, but also for potential device applications in electronics, spintronics, and optoelectronics[8–14]. Several novel characteristics of TCIs have been revealed by surface sensitive probes[3–6, 12]. However, the transport and optical properties of the (001) SS, which are fundamentally important and arguably most relevant to applications[8–14], have remained especially challenging to measure because of the overwhelming effects of bulk carriers in previous studies[15–17]. This has seriously hampered the progress in this field.

Here, we present infrared (IR) reflectance measurements of a TCI, Pb$_{1-x}$Sn$_x$Se ($x = 0.23–0.25$) single crystals with (001) surface in zero and high magnetic fields. From the band gap, Fermi velocity and Fermi energy of the bulk bands determined from our data, the bulk Drude spectral weight (SW) can be estimated, which is found to be much less than the measured Drude weight, indicating substantial contributions from surface carriers. Secondly, the spectral features in magneto-reflectance spectra below 25 meV can be attributed to a dominant resonance at $\omega_c^{ss} \propto B$ based on theoretical study of cyclotron resonance (CR) of the SS, the frequency of which obtained from our data (ω_c^{ss}) is quantitatively consistent with those estimated from previous scanning tunneling microscopy (STM) and angle-resolved photoemission spectroscopy (ARPES) experiments. Moreover, the SW of the dominant resonance in magnetic field is in accord with the extra Drude weight in zero field besides the bulk contribution. Above all, we demonstrate that the resonance at ω_c^{ss} in field is well below the energy range of all Landau level (LL) transitions (including CR) from the bulk states, so it can only be assigned to the SS. Therefore, all these findings taken together provide robust evidence for SS in Pb$_{1-x}$Sn$_x$Se. Remarkably, we find that the IR conductivity of Pb$_{1-x}$Sn$_x$Se is dominated by the SS in the far-IR range (7–25 meV or 2–6 THz) despite the presence of bulk

carriers. We show that this unexpected property arises from the unique band structure of the SS and the resultant high surface carrier density and small IR penetration depth. Furthermore, our experiments yield a surface mobility of ~40,000 cm^2 V^{-1} s^{-1} based on analysis of CR mode of the SS, which is 1–2 orders of magnitude higher than that in TCI thin films[21–23] and among the highest reported values in topological materials. The ultrahigh surface mobility and other transport parameters obtained here suggest that surface-dominated transport can be achieved in (001)-oriented Pb$_{1-x}$Sn$_x$Se crystals with sub-micron thickness. Our findings open up opportunities for exploring many exotic transport and optical phenomena and applications predicted for TCIs[8–14], ranging from quantum anomalous Hall effect and Weyl fermions to spintronics and valleytronics.

Results

IR spectra of Pb$_{1-x}$Sn$_x$Se. In this work, Pb$_{1-x}$Sn$_x$Se single crystals with an actual composition of $x = 0.23–0.25$ were investigated, which are in the TCI phase and host gapless SS[4] (Fig. 1a). The actual composition is determined from the bulk band gap[4] as discussed below. These materials have a direct bulk band gap located at four L points (valleys) in the three-dimensional (3D) Brillouin zone. Our samples are n-doped with the Fermi energy E_F in the bulk conduction band[3]. The IR reflectance spectra $R(\omega)$ of Pb$_{1-x}$Sn$_x$Se crystals with (001) surface were measured in zero field and in magnetic field applied perpendicular to the surface of the samples. Figure 1 depicts the $R(\omega)$ spectrum and the dissipative part of the optical conductivity $\sigma_1(\omega)$ in zero field at T = 8 K (see "Methods"). The $R(\omega)$ spectrum shows a typical metallic behavior: $R(\omega)$ is very close to 1 below 15 meV; at higher energy the reflectance is gradually depressed toward a plasma minimum at about 30 meV, followed by a peak around 120 meV. The energy of the plasma minimum observed here is much lower than those in earlier IR studies[16, 17], indicating much lower total carrier density in our samples due to low density of Se vacancy defects (see "Methods" and Supplementary Note 1). The zero field $\sigma_1(\omega)$ spectrum exhibits a Drude component below 25 meV and a threshold-like feature around 100 meV. The narrow plasma minimum in $R(\omega)$ with a half width ~3 meV is a direct manifestation of the very narrow Drude peak in $\sigma_1(\omega)$, which is corresponding to a very low scattering rate. The threshold feature in $\sigma_1(\omega)$ can be assigned to the onset of inter-band transitions for the bulk around $E_{inter} \approx \Delta + E_F \left(1 + \frac{m_c}{m_v}\right)$ as illustrated in the *inset* of Fig. 1c, where Δ is the bulk band gap, the Fermi energy E_F is defined with respect to the bottom of the conduction band, m_c and m_v are effective masses of the conduction and valence band, respectively. The experimental absorption coefficient spectrum
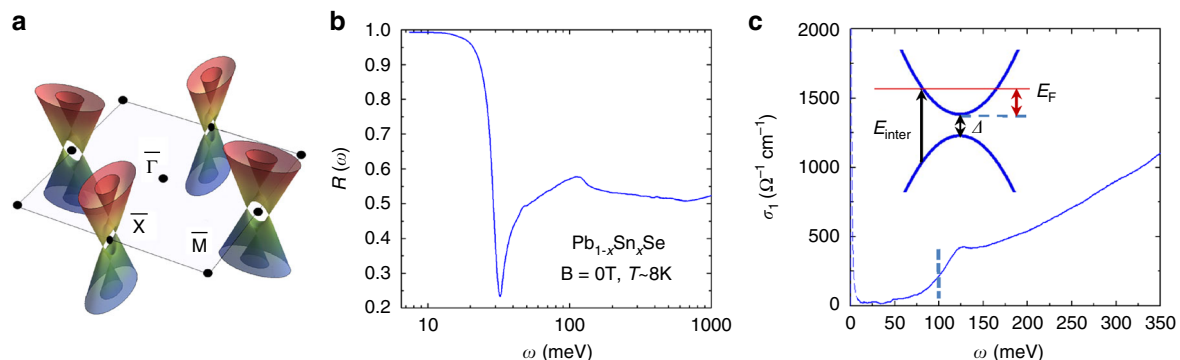
Fig. 1 IR spectra of Pb$_{1-x}$Sn$_x$Se ($x = 0.23–0.25$) in zero magnetic field. **a** Schematic band structure of the SS and the surface Brillouin zone. **b** IR reflectance spectrum $R(\omega)$ at $T = 8$ K. **c** The real part of the optical conductivity $\sigma_1(\omega)$ at $T = 8$ K. The *vertical dashed line* around 100 meV indicates E_{inter}. The *inset* shows a schematic of the band structure of the bulk states and the onset of inter-band transitions at E_{inter}
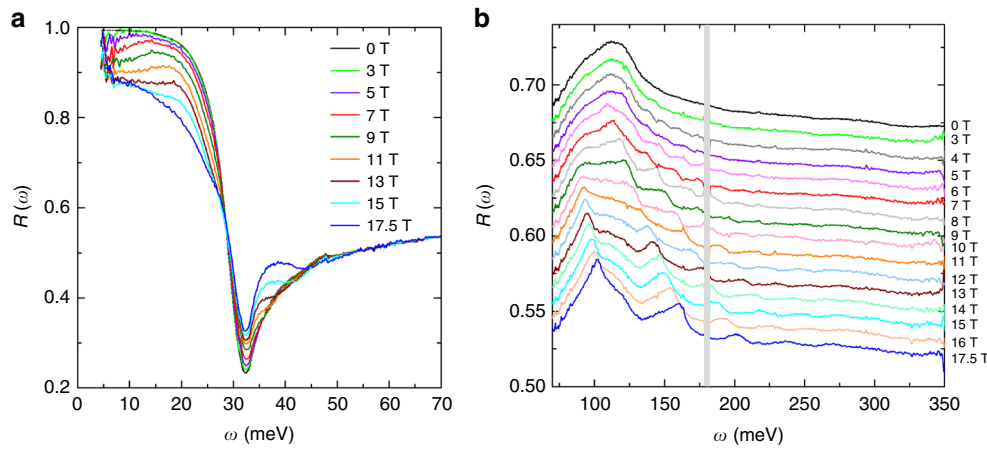
Fig. 2 IR reflectance spectra in magnetic fields. **a**, **b** Reflectance spectra $R(\omega, B)$ in several magnetic fields at T~4.5 K. For clarity the spectra in **b** are displaced from one another by 0.01 with the spectrum at $B = 17.5$ T shown at its actual value. The *gray area* around 175 meV is the energy range in which no data can be obtained due to the absorption of the optical window in our setup

also exhibits a similar threshold feature in the same energy range. It is shown that in doped semiconductors the absorption coefficient can be written as[24, 25] $\alpha(\omega) \propto \alpha_0(\omega)[1 - f(\omega, E_F, T)]$, where $\alpha_0(\omega) \propto \sqrt{\hbar\omega - \Delta/\hbar\omega}$ is the absorption coefficient for the undoped material, $f(\omega, E_F, T) = \left[1 + \exp\left(\frac{\hbar\omega - E_{inter}}{(1 + \frac{m_c}{m_v})k_B T}\right)\right]^{-1}$ is the Fermi distribution, $\hbar$ is Planck's constant divided by 2π, k_B is the Boltzmann constant. Fitting the experimental absorption coefficient using the equation above, we find E_{inter}~100 meV as indicated by the *dashed line* in Fig. 1c.

More insights into the band structure of $Pb_{1-x}Sn_xSe$ can be provided by a systematic investigation of the magneto-reflectance $R(\omega, B)$ spectra displayed in Fig. 2 (see "Methods"). Strikingly, the zero field $R(\omega)$ spectrum is strongly modified by a magnetic field. The $R(\omega, B)$ spectra are strongly suppressed below 25 meV in magnetic fields and no longer extrapolate to unity in the limit of $\omega \to 0$. Moreover, a series of new resonance features are observed in $R(\omega, B)$ extending up to 300 meV, all of which evolve systematically with magnetic fields. In order to acquire a complete understanding of the features in $R(\omega, B)$ spectra, the optical conductivity in magnetic field was extracted from an analysis of $R(\omega, B)$ using the magneto-Drude-Lorentz model[26–28] (see "Methods"). Figure 3a depicts the real part of the optical conductivity Re $\sigma_{xx}(\omega, B)$ from 50 to 300 meV, which exhibit several resonance (absorption) peaks systematically shifting to higher energies with increasing magnetic field. The energies (E) of the absorption features in Re $\sigma_{xx}(\omega, B)$ are displayed in Fig. 3b, which show good agreement with the energies of the resonance features in $R(\omega, B)$. The field-dependent absorption features can be assigned to LL transitions. Interestingly, the observed transitions are not equally spaced in energy in any spectrum, which is in stark contrast to the behavior of systems with quadratic energy-momentum dispersion. We find that the observed resonance features in Re $\sigma_{xx}(\omega, B)$ can be well described by LL transitions of 3D massive Dirac fermions[8, 15], whose LL energies have the form:

$$E_n(k_z) = \pm \delta_{n,0}\sqrt{(\Delta/2)^2 + (\hbar v_F k_z)^2} + \text{sgn}(n)\sqrt{2e\hbar v_F^2 B|n| + (\Delta/2)^2 + (\hbar v_F k_z)^2} \tag{1}$$

which have two zeroth LLs labeled as $n = +0$ and $n = -0$. Here, the integer n is LL index, k_z is momentum along the direction of the magnetic field, e is the elementary charge, v_F is the Fermi velocity, δ is the Kronecker delta function, and sgn(n) is the sign function. Theoretical studies showed that the optical conductivity

has sharp peaks at energies of LL transitions at $k_z = 0$ because of singularities in the joint-density-of-states between LLs at these energies[29]. From the selection rule[29, 30] for allowed optical transitions from LL_n to $LL_{n'}$, $\Delta n = |n| - |n'| = \pm 1$, we find that all the observed resonances can be assigned to allowed LL transitions based on Eq. (1) with $k_z = 0$, $\Delta \approx 64 \pm 3$ meV, and $v_F \approx (0.400 \pm 0.005) \times 10^6$ m s^{-1} (Fig. 3b, c), which are determined from least squares fit of the observed transition energies. This analysis shows that the sharp resonances in Fig. 3a mainly arise from massive Dirac fermions of the bulk states[8, 15]. Since the Sn substitution level directly leads to changes in the bulk band gap, the actual composition of our samples can be determined from Δ to be $x = 0.23 - 0.25$[4].

IR signatures of SS. Our data allow us to identify the signatures of SS in $Pb_{1-x}Sn_xSe$ because all spectroscopic features of the bulk states can be determined. The first evidence for the SS is from an analysis of the Drude SW (area under $\sigma_1(\omega)$) in zero field. The low-energy bulk states can be described by massive Dirac fermions: $E(k) = \pm\sqrt{\hbar^2 v_F^2 k^2 + (\Delta/2)^2}$, with Δ and v_F given above. We can estimate E_F of the bulk states from $E_{inter} \approx \Delta + 2E_F$ (note that $m_c = m_v$ for massive Dirac fermions) shown in Fig. 1c. Alternatively, the transition $LL_{-0} \to LL_{+1}$ disappears at $B < 6$ T (Figs. 2, 3), so the Fermi energy can be estimated as $E_F \sim LL_{+1}(B = 6$ T$) - \Delta/2$ using Eq. (1). Either method yields $E_F \approx 17 \pm 2$ meV. From the band dispersion and E_F, we obtain $k_F \approx 0.014 \pm 0.001$ Å^{-1}. Recent transport studies found that the bulk Fermi surface pockets of $Pb_{1-x}Sn_xSe$ in the TCI phase are nominally spherical[15], so the bulk carrier density can be estimated by $n_{bulk} = \frac{1}{(2\pi)^3}\frac{4}{3}\pi k_F^3 g_s g_v \approx (3.7 \pm 1.1) \times 10^{17}$ cm^{-3}, where $g_s = 2$ and $g_v = 4$ are the bulk spin and valley degeneracy, respectively. Similarly low carrier density has been reported by previous transport experiments[15]. Moreover, the effective mass of massive Dirac fermions at E_F can be calculated from $m_{bulk} = \frac{E_F + \Delta/2}{v_F^2} \approx 0.054 \pm 0.003 m_e$, where m_e is bare electron mass. The SW of the Drude absorption is related to the bare plasma frequency $\omega_P^2 = 4\pi e^2 n/m$ by[31]:

$$\text{SW} = \int_0^{\omega_0} \sigma_1(\omega)d\omega = \frac{\pi\Omega^{-1}}{120}\omega_P^2 \tag{2}$$

where ω_0 is a cut-off frequency separating the Drude component from the inter-band transitions, Ω is Ohm, σ_1 is in
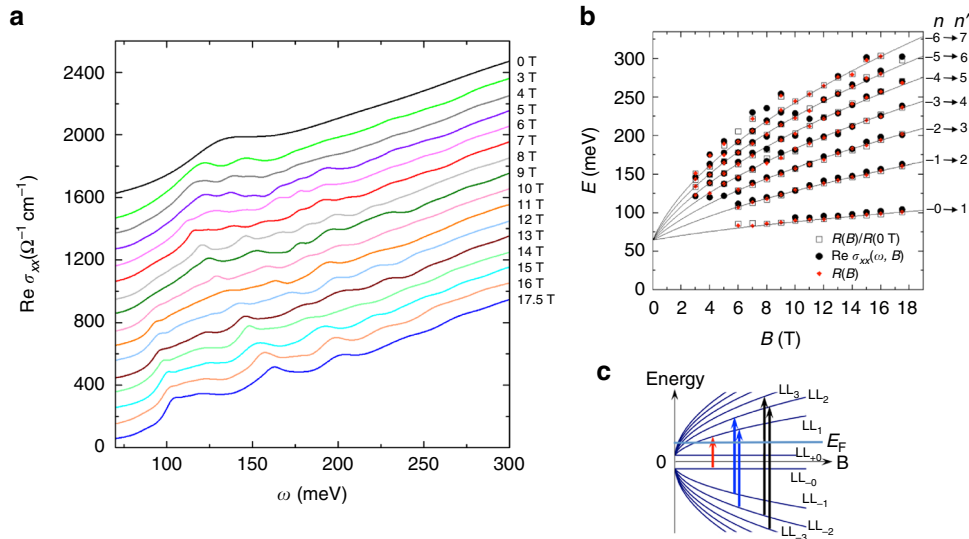
Fig. 3 LL transitions of bulk states. **a** The real part of the optical conductivity Re $\sigma_{xx}(\omega)$ in several magnetic fields. For clarity the spectra are displaced from one another by 100 with the spectrum at $B = 17.5$ T shown at its actual value. **b** The energies of the observed transitions as a function of magnetic field. *Symbols*: data. *Solid lines*: fits to the data using Eq. (1) discussed in the text with $\Delta = 64.5$ meV and $v_F = 0.4 \times 10^6$ m s^{-1}. The observed resonances can be assigned to LL transitions T$_n$, which is due to transitions LL$_{-(n-1)} \rightarrow$ LL$_n$ and LL$_{-n} \rightarrow$ LL$_{n-1}$ for $n > 1$ and LL$_0 \rightarrow$ LL$_1$ for $n = 1$. **c** Schematic of LLs of the bulk states. The *arrows* illustrate T$_1$–T$_3$ shown in **b**

Ω^{-1} cm^{-1}, and all frequencies are in cm^{-1}. From n_{bulk}, m_{bulk}, and Eq. (2), we estimate that SW$_{\text{bulk}} \approx (1.6 \pm 0.5) \times 10^4 \Omega^{-1}$cm^{-2} for the bulk states from calculating $\omega_{\text{P, bulk}}$. On the other hand, the total Drude SW can be determined by the total plasma frequency ω_P of the Drude component in the experimental data using SW$_{\text{total}} = \frac{\pi \Omega^{-1}}{120} \omega_P^2$, where ω_P is related to the screened plasma frequency $\tilde{\omega}_P$ by $\omega_P = \tilde{\omega}_P \sqrt{\varepsilon_\infty}$, with $\tilde{\omega}_P \sim 260$ cm^{-1} (32.4 meV) corresponding to the plasma minimum in $R(\omega)$ and ε_∞ representing all electronic contributions to the dielectric constant other than the Drude component. Therefore, the total plasma frequency ω_P can be obtained from ε_∞, which is determined by all Lorentzian oscillators obtained from Drude-Lorentz fit of the entire $R(\omega)$ spectrum (see Supplementary Note 5). We find that $\varepsilon_\infty \sim 45 \pm 9$, so SW$_{\text{total}} \approx (7.9 \pm 1.6) \times 10^4 \Omega^{-1}$ cm^{-2}. A comparison between SW$_{\text{bulk}}$ and SW$_{\text{total}}$ shows that the bulk contribution can only account for about 20% of the total Drude SW of the system. We emphasize that the total Drude SW and that from bulk states are both accurately determined from our data, which strongly suggests dominant surface contribution to the total Drude absorption in zero field.

The low-energy magneto-reflectance of Pb$_{1-x}$Sn$_x$Se provides further evidence for the SS. The systematic suppression of $R(\omega, B)$ spectrum with B field below 25 meV suggests that the system becomes more insulating with increasing field. This is reminiscent of the typical behavior of CR. For instance, similar low-energy behaviors in $R(\omega, B)$ were also observed in graphite[27] due to CR, which manifests itself in Re $\sigma_{xx}(\omega)$ as a peak at energies of $E \propto B$. We now show that the spectral feature below 25 meV in $R(\omega, B)$ and its evolution with B field are unambiguous signatures of CR from the SS (Supplementary Notes 2 and 3). As shown in Figs. 1a and 4a, the band structure of SS on the (001) surface features two generations of Dirac fermions[7], starting from a pair of Dirac cones located at the $\overline{X}$ points of the surface Brillouin zone with their Dirac points at $E_{\text{H1}}^{\text{DP}}$ and $E_{\text{H2}}^{\text{DP}}$. The hybridization between these two Dirac cones leads to a gap in all directions except along the $\overline{\Gamma X}$ line (Fig. 1a), where a pair of Dirac points exist that are protected by the (110) mirror symmetry[2, 7]. Recent experiments and theoretical calculations[3, 32, 33] suggest that $E_{\text{H1}}^{\text{DP}}$ is close to E_F of the bulk states for Pb$_{1-x}$Sn$_x$Se. In a magnetic field

perpendicular to the surface, it is shown[32] that the LLs of the SS near E_F are well approximated by LLs of two independent Dirac cones at $E_{\text{H1}}^{\text{DP}}$ and $E_{\text{H2}}^{\text{DP}}$ (Fig. 4b), which have energies of

$$E_n = \text{sgn}(n) \sqrt{2e\hbar (\bar{v}_F^{\text{SS}})^2 B |n|}$$

with respect to each Dirac point and $\bar{v}_F^{\text{SS}} \sim 0.4 \times 10^6$ m s^{-1}[3, 32, 33]. Within this picture, a CR mode due to the intra-band LL transition associated with the Dirac cone at $E_{\text{H2}}^{\text{DP}}$ is expected at low energy (Fig. 4b). The surface Fermi energy with respect to $E_{\text{H2}}^{\text{DP}}$ is estimated to be $E_F^{\text{SS}} \sim 136 \pm 14$ meV based on STM and ARPES experiments[3, 32, 33], from which the energy of the surface CR mode is expected to be $\omega_c^{\text{ss}} = eB/m_{ss}$ with $m_{ss} = E_F^{\text{SS}}/(\bar{v}_F^{\text{SS}})^2 = 0.15 \pm 0.015$ m_e. LL transitions of SS associated with the Dirac cone at $E_{\text{H1}}^{\text{DP}}$ can also contribute to the $R(\omega, B)$ spectra at $\sqrt{2e\hbar (\bar{v}_F^{\text{SS}})^2 B}$ or higher energy, but it is very difficult to separate them from bulk LL transitions that are in the same energy range. It is shown[32] that LLs associated with the Dirac cone along the $\overline{\Gamma X}$ line are restricted in the energy range between E_{VHS1} and E_{VHS2} in Fig. 4a, b, so these LLs below E_F cannot be probed from optical measurements, which requires optical transitions from a LL below E_F to one above E_F. To examine the IR signatures of the surface CR mode, the magneto-Drude-Lorentz model is used to simulate the $R(\omega, B)$ spectra (see "Methods"). The real and imaginary parts of $\sigma_{xx}(\omega)$, $\sigma_{xy}(\omega)$, $\sigma_+(\omega)$, and $\sigma_-(\omega)$ in representative models are displayed and discussed in Supplementary Note 2. We find that the principle features of $R(\omega, B)$ can be reproduced by model optical conductivity spectra that are based on the expected behaviors of the surface CR mode[32]: remarkably, a strong resonance peak at ω_c^{ss} in Re $\sigma_{xx}(\omega, B)$ that changes linearly with B field (Fig. 4c) can capture the spectral feature in $R(\omega, B)$ below 25 meV and its evolution with B field. In particular, the analysis on our data yields m_{ss} values in the range of 0.15–0.19 m_e for the CR mode, which are consistent with those estimated from STM and ARPES experiments[3, 33] within 15% as shown in Fig. 4d (see Supplementary Note 2). The small deviation between our results and STM and ARPES measurements may arise from the difference in Fermi energy in different samples. Based on LL
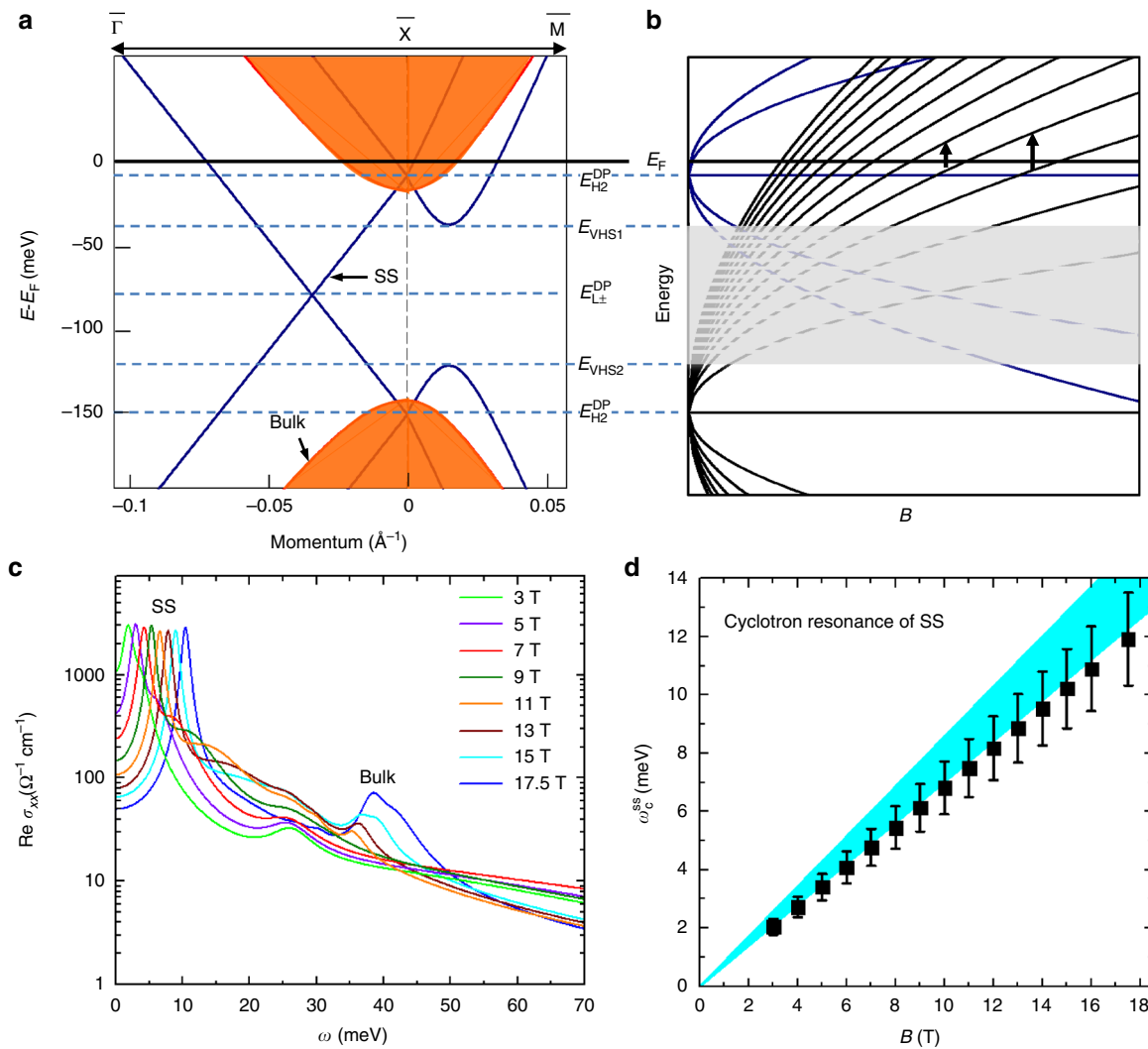
Fig. 4 IR conductivity of SS in magnetic fields. **a** A schematic of the SS band structure (*dark blue*) and that of the bulk (*red*) along two high-symmetry directions for one of the four Dirac cones inside the surface Brillouin zone. E_{H1}^{DP}, E_{H2}^{DP}, and $E_{L\pm}^{DP}$ are energies of the Dirac points associated with the two Dirac cones located at the $\overline{X}$ points and the Dirac nodes along the $\overline{\Gamma X}$ line, respectively. E_{VHS1} and E_{VHS2} are energies of the two Van Hove singularities in the band structure. **b** A schematic of LLs of the SS in the same energy scale as that in **a**. While the LLs between E_{VHS1} and E_{VHS2} in the *gray-shaded area* have nontrivial dispersions[32] (not shown here), the LLs near E_F are well approximated by LLs of two independent Dirac cones at E_{H1}^{DP} and E_{H2}^{DP} as illustrated by the *dashed lines* in the *shaded* area. The CR of the SS associated with the Dirac cone at E_{H2}^{DP} is shown by the *vertical arrows*. **c** The real part of the model optical conductivity Re $\sigma_{xx}(\omega)$ in several magnetic fields that are used to simulate the $R(\omega, B)$ spectra below 70 meV. The strong peak below 15 meV in Re $\sigma_{xx}(\omega)$ arises from CR of the SS, which represents the spatially averaged 3D optical conductivity of the SS within the IR penetration depth. **d** The CR energy of SS ω_c^{ss} as a function of magnetic field. The *error bars* represent the range of ω_c^{ss} values that can be used in our model to produce excellent fit of the $R(\omega, B)$ data within experimental uncertainties as discussed in Supplementary Note 2. The *shaded area* indicates the range of ω_c^{ss} values estimated from previous STM and ARPES experiments

energies calculated from Δ and ν_F for the bulk and Eq. (1), the peak between 30 and 50 meV in Re $\sigma_{xx}(\omega)$ spectra can be assigned to the $LL_{+0} \rightarrow LL_{+1}$ transition (intra-band LL transition or CR) from the bulk states for $B > 6$ T, which is responsible for the feature around 37 meV in $R(\omega, B)$. Because E_F is between LL_{+0} and LL_{+1} above $B \sim 6$ T, the bulk CR $LL_{+0} \rightarrow LL_{+1}$ around 37 meV has the lowest energy among all allowed LL transitions for the bulk for $B > 6$ T (Fig. 3c). Therefore, the spectral feature in $R(\omega, B)$ below 25 meV can only be assigned to the SS, because it is well below the energy range of all LL transitions (including CR) from the bulk states for $B > 6$ T. Moreover, from the area under the resonance at ω_c^{ss} in Re $\sigma_{xx}(\omega)$, the SW of this resonance is found to be $SW_{SS} \sim (4.4 \pm 0.9) \times 10^4 \, \Omega^{-1} \, cm^{-2}$, which is in agreement with the extra Drude SW in zero field besides the bulk contribution $\sim (6.3 \pm 2.1) \times 10^4 \, \Omega^{-1} \, cm^{-2}$. This agreement

provides further support for our identification of the surface CR mode. Therefore, our data in zero and high magnetic fields taken together provide robust evidence for the IR signatures of SS in $Pb_{1-x}Sn_xSe$.

SS dominated far-IR conductivity. Strikingly, the far-IR conductivity of (001)-oriented $Pb_{1-x}Sn_xSe$ is dominated by the SS in the energy range of the Drude absorption in zero field and that of the surface CR mode in magnetic field, which is around 7–25 meV or 2–6 THz. We now show that this is a consequence of the unique band structure of the (001) SS. The SS of our n-doped samples has two Fermi surfaces associated with the two Dirac cones at E_{H1}^{DP} and E_{H2}^{DP} (Fig. 4a). In particular, the latter Dirac cone gives rise to a large Fermi surface with $\overline{k}_F^{SS} \sim$

$E_F^{SS}/(\hbar \overline{v}_F^{SS}) \sim 0.052 \pm 0.005$ Å^{-1} [3, 32, 33]. Neglecting the small contribution from the Fermi surface associated with the Dirac cones at E_{H1}^{DP} and taking into account $g_s = 1$ and $g_v = 2$ for the SS, we estimate that the large SS Fermi surface leads to a very high surface carrier density $n_{SS}^{2D} \sim (4.2 \pm 0.8) \times 10^{12}$ cm^{-2}, which is more than one order of magnitude higher than that of the (111) surface in TCIs[21, 34]. The large value of n_{SS}^{2D} of the (001) surface is critical for achieving surface dominated far-IR conductivity in Pb$_{1-x}$Sn$_x$Se despite the presence of bulk carriers. Our measurements only probe the region of the sample within the IR penetration depth δ. An estimate for the length scale of δ for our samples between 7 and 25 meV can be obtained from a SW analysis. The Drude weight of the (001) SS can be estimated as $e^2 E_F^{SS} g_s g_v/(8\hbar^2)$[35], which only includes contributions from the massless Dirac fermions associated with the Dirac cone at E_{H2}^{DP}. The same surface Drude weight can be obtained from SW$_{SS}\delta$ based on our IR measurements, so the averaged length scale of δ between 7 and 25 meV is estimated to be 13 ± 4 nm for our samples. It can be shown that δ is comparable to the penetration depth of the SS (see "Methods"). This suggests that the high-carrier density of the (001) SS leads to strong IR absorption and attenuates the IR light within a very small penetration depth, which effectively reduces the bulk contribution to the far-IR conductivity. It is instructive to compare our results with a recent IR study of (111)-oriented TCI thin films[34], which reported substantially lower surface SW compared to the bulk contribution. It is found that the (111) surface carrier density is ten times lower and the IR penetration depth is much larger than those in our samples[34], owing to a much smaller k_F for the (111) SS. These results are consistent with our findings that the high surface carrier density reduces the IR penetration depth and thus the bulk contribution to the overall far-IR conductivity in (001)-oriented Pb$_{1-x}$Sn$_x$Se. Therefore, the unique band structure of (001) SS plays a crucial role in achieving surface-dominated far-IR conductivity observed in our study. The large difference in the IR properties of (001) and (111) surfaces is a new aspect in TCIs compared to those in Z_2 topological insulators[36–39].

Discussion

Our study sheds new light on the mobility of the (001) SS of Pb$_{1-x}$Sn$_x$Se. From half width of the surface CR mode in Re $\sigma_{xx}(\omega)$, the scattering rate of the SS is estimated to be $1/\tau_{SS} \sim 1.2 \pm 0.6$ meV, which clearly manifest itself as the very narrow dip feature around 32 meV in $R(\omega, B)$ (Supplementary Note 4). Therefore, the mobility of the SS can be estimated: $\mu_{SS} = e\overline{v}_F^{SS}\tau_{SS}/(\hbar \overline{k}_F^{SS}) = e\tau_{SS}/m_{SS} \sim 40,000$ cm^2 V^{-1} s^{-1} with an uncertainty of about 50%. Such a high surface mobility is very promising for studying the intrinsic physics of TCIs. Detailed analysis on the scattering rate and mobility from previous IR study of LL transitions in graphene[40] support our estimation of surface mobility in TCIs since both systems feature massless Dirac fermions (Supplementary Note 4). In contrast, previous studies on TCI thin films reported surface mobility values in the range of 100–2000 cm^2 V^{-1} s^{-1}[21–23] and a broad surface IR absorption feature that is ten times wider than that in our data[34]. The low mobility values of these TCI thin films are very likely limited by sample quality. We note that the small scattering rate and high mobility of the (001) SS also play an important role in leading to strong surface absorption in a narrow energy range in far-IR and thus a small IR penetration depth, which is responsible for the observed surface-dominated IR conductivity.

A long-standing challenge in the research of TCIs as well as Z_2 topological insulators is to realize surface-dominated

transport[41–45]. Our study elucidates the surface and bulk contributions to electronic transport. From the effective mass of bulk states m_{bulk} obtained from zero-field data and the scattering rate estimated from bulk LL transitions $1/\tau_{bulk} \sim 10$ meV, the bulk mobility of our samples can be estimated: $\mu_{bulk} \sim 13,000$ cm^2 V^{-1} s^{-1}. Similarly high mobility has been reported by previous transport experiments[15]. For a sample with thickness d, the fraction of surface contribution to the total conductance can be estimated as $n_{SS}^{2D}\mu_{SS}e/(n_{SS}^{2D}\mu_{SS}e + n_{bulk}d\mu_{bulk}e)$. The mobility and carrier density values obtained in our study suggest that the SS in our samples will contribute to more than 50% of the total conductance in crystals with $d < 0.4$ μm. Surface-dominated transport can be achieved in even thicker crystals if the bulk carrier density is reduced further in future.

In conclusion, our study has revealed several IR signatures of SS in Pb$_{1-x}$Sn$_x$Se, including their contribution to the Drude absorption in zero field and their CR mode in magnetic field, whose SWs are further found to be consistent. Moreover, the frequency of the surface CR mode ω_c^{ss} inferred from our data is in accord with those estimated from theoretical studies and STM and ARPES measurements. Finally, we show that the resonance at ω_c^{ss} in field can only be assigned to the SS, because it is well below the energy range of all bulk LL transitions. Our study demonstrates the viability of surface-dominated IR conductivity and transport, as well as an ultrahigh surface mobility of ~40,000 cm^2 V^{-1} s^{-1} in Pb$_{1-x}$Sn$_x$Se with (001) surface. We expect that these results can be found in a broad class of IV–VI semiconductor TCIs Pb$_{1-x}$Sn$_x$Se(Te) because of the similar properties of their SS[1–8]. These findings establish Pb$_{1-x}$Sn$_x$Se(Te) thin crystals (potentially with electrostatic gating) as a fertile system for accessing the optical and transport properties of the (001) SS, which is a crucial step for exploring many novel topological phenomena in TCIs and their potential electronic, spintronic, and valleytronic applications[8–14].

Methods

IR measurements and data analysis. Pb$_{1-x}$Sn$_x$Se ($x = 0.23$–0.25) single crystals with centimeter size were grown by the Bridgman growth method. As Pb$_{1-x}$Sn$_x$Se crystals have cubic symmetry, the samples in our study have been chosen from naturally cleaved cubic crystals with easy low indexing (00L) cleavage planes. The carrier density in the crystals is batch (growth)-dependent even for the same nominal Pb/Sn ratio because of the self-doping effect of Se vacancy defects (see Supplementary Note 1). The crystals used in our IR study are from a batch with low-carrier (defect) density. The samples were cleaved in ambient conditions before the first IR measurement, and their exposure time in air was minimized between subsequent measurements. The zero-field reflectance spectrum $R(\omega)$ was measured in the energy range of 7.5–900 meV at a temperature of T = 8 K. The magneto-reflectance ratio spectra $R(\omega, B)/R(\omega, B = 0$ T) were measured at T~4.5 K in a superconducting magnet in the Faraday geometry (magnetic field perpendicular to the sample surface). The $R(\omega, B)$ spectra were obtained by multiplying the magneto-reflectance ratio spectra by $R(\omega)$ at zero field (Supplementary Note 1). We estimate the experimental uncertainty of the absolute values of $R(\omega, B)$ is about 1–1.5%, but the relative change (evolution) of $R(\omega, B)$ with magnetic field has a smaller uncertainty owing to the better accuracy of the magneto-reflectance ratio data.

As an approximation for exploring spatially averaged properties of the SS, our data analysis employs a model with uniform carrier density n_{SS} for the SS without a sharp surface/bulk interface, which will be elaborated below. In such a model, the IR data can be analyzed using formulas for bulk materials and the resulting optical conductivity contains contributions from both the SS and bulk, with all quantities of the SS being spatially averaged ones along the direction perpendicular to the surface within the IR penetration depth. The complex optical conductivity $\sigma(\omega) = \sigma_1(\omega) + i\sigma_2(\omega)$ in zero field at 8 K was obtained from analysis of $R(\omega)$ using Drude-Lorentz model combined with Kramers-Kronig (KK) constrained variational dielectric functions[28]. Alternatively, $\sigma(\omega)$ in zero field can be obtained from KK transformation of $R(\omega)$ data, in which Hagen–Rubens formula was employed in the low-energy region and the $R(\omega)$ data at 8 K was extend to 5.765 eV using room temperature reflectance data. The two approaches above yield consistent $\sigma(\omega)$ spectra with identical spectral features. In magnetic field, the R(ω, B) spectra were analyzed using magneto-Drude-Lorentz model[26], in which the optical conductivity for right and left circularly polarized light (denoted + and −, respectively) is given

by:

$$\sigma_{\pm}(\omega) = \frac{\omega}{4\pi i}\left(\varepsilon_{\infty}^{B} - 1 + \sum \frac{\omega_{p,n}^2}{\omega_{o,n}^2 - \omega^2 - i\gamma_n\omega \mp \omega_{c,n}\omega}\right) \quad (3)$$

where $\omega_{p,n}$, $\omega_{o,n}$, γ_n, and $\omega_{c,n}$ are the plasma frequency, energy, linewidth, and cyclotron energy of the n-th oscillator, respectively. ε_{∞}^{B} represents high-energy contributions to the dielectric constant from energy range higher than all the oscillators. In our analysis, we choose $\omega_{o,n} = 0$ for all oscillators. The magneto-Drude-Lorentz model ensures that the real and imaginary parts of optical conductivity are constrained by KK relations, therefore it is commonly used to describe LL transitions including CR. The xx and xy components of the optical conductivity are: $\sigma_{xx}(\omega) = [\sigma_{+}(\omega) + \sigma_{-}(\omega)]/2$, $\sigma_{xy}(\omega) = [\sigma_{+}(\omega) - \sigma_{-}(\omega)]/2i$. The dielectric function is $\varepsilon_{\pm}(\omega) = 1 + \frac{4\pi i \sigma_{\pm}(\omega)}{\omega}$. The complex reflectivity is given by $r_{\pm}(\omega) = \frac{1 - \sqrt{\varepsilon_{\pm}(\omega)}}{1 + \sqrt{\varepsilon_{\pm}(\omega)}}$. Finally, the measured reflectance spectrum is given by:

$$R(\omega) = \frac{|r_{+}(\omega)|^2 + |r_{-}(\omega)|^2}{2} \quad (4)$$

The experimental $R(\omega, B)$ data were fit with model reflectance spectrum calculated from Eq. (4). In principle, a complete determination of both $\sigma_{+}(\omega)$ and $\sigma_{-}(\omega)$ cannot be achieved without Kerr rotation measurements. However, after trying numerous versions of $\sigma_{+}(\omega)$ and $\sigma_{-}(\omega)$ to fit $R(\omega, B)$, we find that good fits always yield quite similar Re $\sigma_{xx}(\omega)$ spectra in the energy range of 75–350 meV. Qualitatively, because of the small changes in $R(\omega, B)/R(\omega, B = 0\,\text{T})$ (less than 5%) and the relatively flat spectral feature in $R(\omega, B = 0\,\text{T})$ in 75–350 meV, the resonances in $R(\omega, B)$ are mathematically related to peaks in Re $\sigma_{xx}(\omega)$ at very similar energies, which allows us to determine Re $\sigma_{xx}(\omega)$ with good accuracy in this energy range. On the other hand, due to the strong energy dependence of the spectral features in $R(\omega, B = 0\,\text{T})$ below 50 meV and much larger changes in $R(\omega, B)/R(\omega, B = 0\,\text{T})$ (~20%), it is impossible to accurately determine Re $\sigma_{xx}(\omega)$ in the low-energy range. Therefore, we use one oscillator at ω_c^{ss} based on theoretical results on the CR of the SS in TCIs[32] and several much weaker oscillators to simulate the $R(\omega, B)$ spectra below 60 meV, employing the magneto-Drude-Lorentz model. While our discussions are mainly focused on the Re $\sigma_{xx}(\omega)$ spectrum, the real and imaginary parts of $\sigma_{xx}(\omega)$, $\sigma_{xy}(\omega)$, $\sigma_{+}(\omega)$, and $\sigma_{-}(\omega)$ in representative models are displayed and discussed in Supplementary Note 2.

Our model is a good approximation for investigating $Pb_{1-x}Sn_xSe$ ($x = 0.23$–0.25), which has a large SS penetration depth. The length scale of the penetration depth (spatial spread) of the SS into the bulk can be estimated as $\lambda_{SS} \sim \hbar v_F^{SS}/\Delta$, where v_F^{SS} is the Fermi velocity of the Dirac fermions of the SS and Δ is the bulk band gap[12]. λ_{SS} can be large for small values of Δ and even goes to infinity with $\Delta = 0$. The value of λ_{SS} in $Pb_{1-x}Sn_xSe$ can be estimated from a comparison with topological insulator Bi_2Se_3, whose λ_{SS} has been found to be ~2.5 nm (2.5 quintuple layers)[46]. The bulk band gap for our sample is about 1/5 of that of Bi_2Se_3 and the two materials have quite similar v_F^{SS} values[46], so the length scale of λ_{SS} is expected to be ~12.5 nm. Moreover, theoretical calculations[12] have shown that the percentage of the SS wavefunction in the topmost layer for $Pb_{1-x}Sn_xSe$ ($x = 0.23$–0.25) is ~0.5%, which suggests that λ_{SS} is much larger than 200 layers or 60 nm based on the lattice constant ~0.3 nm. On the other hand, the far-IR range of 7–25 meV is the main focus of our discussions on the SS, where the averaged length scale of the IR penetration depth estimated from our data is δ~13 ± 4 nm, which is comparable to (or smaller than) the length scale of λ_{SS}. Our analysis employs a model with two main approximations: first, both the SS and bulk states exist within the entire IR penetration depth without a sharp surface/bulk interface, which is justified since δ~λ_{SS} in $Pb_{1-x}Sn_xSe$ in the frequency range of interest; second, as an approximation for studying spatially averaged properties of the SS, the model assumes a uniform n_{SS} for the SS. With these approximations the IR data can be analyzed using the methods detailed above. Regarding SS penetration depth, $Pb_{1-x}Sn_xSe$ ($x = 0.23$–0.25) is very different from Z_2 topological insulators; in the latter materials $\lambda_{SS} << \delta$ and the IR data can be analyzed using a multilayer model with distinct surface and bulk layers[45, 47].

Experimental uncertainty analysis. The uncertainties of the band gap Δ and Fermi velocity v_F of the bulk states are estimated based on the variations of their values from fitting different LL transitions and a confidence interval of 95% in the least squares fit. The uncertainty of E_F of the bulk states is estimated from the uncertainties in defining E_{inter} in the $\sigma_1(\omega)$ spectrum or the magnetic field below which the transition $LL_{-0} \rightarrow LL_{+1}$ disappears. The uncertainty of the total Drude SW, SW_{total}, is discussed in Supplementary Note 5. In the analysis for data in magnetic field, the uncertainties of the SW, SW_{SS}, and scattering rate $1/\tau_{SS}$ of the CR mode of the SS represent the range of these parameters that can be used to reproduce the $R(\omega, B)$ data. The uncertainties of all other quantities discussed in the main text are calculated using standard formulas for propagation of uncertainty.

Data availability. The data that support the findings of this study are available from the corresponding author upon reasonable request.

References

1. Fu, L. Topological crystalline insulators. *Phys. Rev. Lett.* **106**, 106802 (2011).
2. Hsieh, T. H. et al. Topological crystalline insulators in the SnTe material class. *Nat. Commun.* **3**, 982 (2012).
3. Okada, Y. et al. Observation of Dirac node formation and mass acquisition in a topological crystalline insulator. *Science* **341**, 1496–1499 (2013).
4. Dziawa, P. et al. Topological crystalline insulator states in $Pb_{1-x}Sn_xSe$. *Nat. Mater.* **11**, 1023–1027 (2012).
5. Xu, S. Y. et al. Observation of a topological crystalline insulator phase and topological phase transition in $Pb_{1-x}Sn_xTe$. *Nat. Commun.* **3**, 1192 (2012).
6. Tanaka, Y. et al. Experimental realization of a topological crystalline insulator in SnTe. *Nat. Phys.* **8**, 800–803 (2012).
7. Liu, J., Duan, W. & Fu, L. Two types of surface states in topological crystalline insulators. *Phys. Rev. B* **88**, 241303 (2013).
8. Ando, Y. & Fu, L. Topological crystalline insulators and topological superconductors: from concepts to materials. *Annu. Rev. Condens. Matter Phys.* **6**, 361–381 (2015).
9. Tang, E. & Fu, L. Strain-induced partially flat band, helical snake states and interface superconductivity in topological crystalline insulators. *Nat. Phys.* **10**, 964–969 (2014).
10. Liu, J. et al. Spin-filtered edge states with an electrically tunable gap in a two-dimensional topological crystalline insulator. *Nat. Mater.* **13**, 178–183 (2014).
11. Fang, C., Gilbert, M. J. & Bernevig, B. A. Large-Chern-number quantum anomalous hall effect in thin-film topological crystalline insulators. *Phys. Rev. Lett.* **112**, 046801 (2014).
12. Ilija, Z. et al. Dirac mass generation from crystal symmetry breaking on the surfaces of topological crystalline insulators. *Nat. Mater.* **14**, 318–324 (2015).
13. Liu, J., Fang, C. & Fu, L. Tunable Weyl fermions and Fermi arcs in magnetized topological crystalline insulators. Preprint at https://arxiv.org/abs/1604.03947 (2016).
14. Ezawa, M. Valleytronics on the surface of a topological crystalline insulator: elliptic dichroism and valley-selective optical pumping. *Phys. Rev. B* **89**, 195413 (2014).
15. Liang, T. et al. Evidence for massive bulk Dirac fermions in $Pb_{1-x}Sn_xSe$ from Nernst and thermopower experiments. *Nat. Commun.* **4**, 2696 (2013).
16. Anand, N. et al. Temperature-driven band inversion in $Pb_{0.77}Sn_{0.23}Se$: optical and Hall effect studies. *Phys. Rev. B* **90**, 235143 (2014).
17. Reijnders, A. A. et al. Optical investigation of the thermoelectric topological crystalline insulator $Pb_{0.77}Sn_{0.23}Se$. *Phys. Rev. B* **90**, 235144 (2014).
18. Hasan, M. Z. & Kane, C. L. Colloquium: topological insulators. *Rev. Mod. Phys.* **82**, 3045 (2010).
19. Qi, X. L. & Zhang, S. C. Topological insulators and superconductors. *Rev. Mod. Phys.* **83**, 1057 (2011).
20. Moore, J. E. The birth of topological insulators. *Nature* **464**, 194–198 (2010).
21. Taskin, A. A., Yang, F., Sasaki, S., Segawa, K. & Ando, Y. Topological surface transport in epitaxial SnTe thin films grown on Bi_2Te_3. *Phys. Rev. B* **89**, 121302 (2014).
22. Assaf, B. A. et al. Quantum coherent transport in SnTe topological crystalline insulator thin films. *Appl. Phys. Lett.* **105**, 102108 (2014).
23. Zhang, C. et al. Highly tunable Berry phase and ambipolar field effect in topological crystalline insulator $Pb_{1-x}Sn_xSe$. *Nano Lett.* **15**, 2161–2167 (2015).
24. Palik, E. D., Mitchell, D. L. & Zemel, J. N. Magneto-optical studies of band structure of PbS. *Phys. Rev.* **135**, A763–A778 (1964).
25. Gibbs, Z. M., LaLonde, A. & Snyder, G. J. Optical band gap and the Burstein-Moss effect in iodine doped PbTe using diffuse reflectance infrared Fourier transform spectroscopy. *New. J. Phys.* **15**, 075020 (2013).
26. Lax, B. & Mavroides, J. G. in *Semiconductors and Semimetals*, Vol. 3 (eds R. Willardson, K. & Beer, A. C.) 321–401 (Academic Press, 1967).
27. Li, Z. Q. et al. Infrared probe of the anomalous magnetotransport of highly oriented pyrolytic graphite in the extreme quantum limit. *Phys. Rev. B* **74**, 195404 (2006).
28. Kuzmenko, A. B. Kramers–Kronig constrained variational analysis of optical spectra. *Rev. Sci. Instrum.* **76**, 083108 (2005).
29. Ashby, P. E. C. & Carbotte, J. P. Magneto-optical conductivity of Weyl semimetals. *Phys. Rev. B* **87**, 245131 (2013).
30. Gusynin, V. P., Sharapov, S. G. & Carbotte, J. P. Magneto-optical conductivity in graphene. *J. Phys. Condens. Matter* **19**, 026222 (2007).
31. Basov, D. N., Averitt, R. D., van der Marel, D., Dressel, M. & Haule, K. Electrodynamics of correlated electron materials. *Rev. Mod. Phys.* **83**, 471 (2011).
32. Serbyn, M. & Fu, L. Symmetry breaking and Landau quantization in topological crystalline insulators. *Phys. Rev. B* **90**, 035402 (2014).
33. Neupane, M. et al. Topological phase diagram and saddle point singularity in a tunable topological crystalline insulator. *Phys. Rev. B* **92**, 075131 (2015).

34. Assaf, B. A. et al. Massive and massless Dirac fermions in $Pb_{1-x}Sn_xTe$ topological crystalline insulator probed by magneto-optical absorption. *Sci. Rep.* **6**, 20323 (2016).

35. Ando, T., Zheng, Y. & Suzuura, H. Dynamical conductivity and zero-mode anomaly in honeycomb lattices. *J. Phys. Soc. Jpn.* **71**, 1318–1324 (2002).

36. Wu, L. et al. High-resolution Faraday rotation and electron-phonon coupling in surface states of the bulk-insulating topological insulator $Cu_{0.02}Bi_2Se_3$. *Phys. Rev. Lett.* **115**, 217602 (2015).

37. Post, K. W. et al. Sum-rule constraints on the surface state conductance of topological insulators. *Phys. Rev. Lett.* **115**, 116804 (2015).

38. Jenkins, G. S. et al. Dirac cone shift of a passivated topological Bi_2Se_3 interface state. *Phys. Rev. B* **87**, 155126 (2013).

39. Hancock, J. N. et al. Surface state charge dynamics of a high-mobility three-dimensional topological insulator. *Phys. Rev. Lett.* **107**, 136803 (2011).

40. Jiang, Z. et al. Infrared spectroscopy of Landau levels of graphene. *Phys. Rev. Lett.* **98**, 197403 (2007).

41. Analytis, J. G. et al. Two-dimensional surface state in the quantum limit of a topological insulator. *Nat. Phys.* **6**, 960–964 (2010).

42. Qu, D. X., Hor, Y. S., Xiong, J., Cava, R. J. & Ong, N. P. Quantum oscillations and Hall anomaly of surface states in the topological insulator Bi2Te3. *Science* **329**, 821–824 (2010).

43. Taskin, A. A., Ren, Z., Sasaki, S., Segawa, K. & Ando, Y. Observation of Dirac holes and electrons in a topological insulator. *Phys. Rev. Lett.* **107**, 016801 (2011).

44. Xu, Y. et al. Observation of topological surface state quantum Hall effect in an intrinsic three-dimensional topological insulator. *Nat. Phys.* **10**, 956–963 (2014).

45. Cheng, B., Wu, L., Kushwaha, S. K., Cava, R. J. & Armitage, N. P. Measurement of the topological surface state optical conductance in bulk-insulating Sn-doped Bi1.1Sb0.9Te2S single crystals. *Phys. Rev. B* **94**, 201117(R) (2016).

46. Zhang, Y. et al. Crossover of the three-dimensional topological insulator Bi_2Se_3 to the two-dimensional limit. *Nat. Phys.* **6**, 584–588 (2010).

47. Reijnders, A. A. et al. Optical evidence of surface state suppression in Bi-based topological insulators. *Phys. Rev. B* **89**, 075138 (2014).

Author contributions

L.F. and Z.L. conceived the research and supervised the project together with F.C.; R.S. and F.C. contributed to the single-crystal growth; Z.L. and N.-L.W. supervised the experiments; Y.W. and Z.L. analyzed the data, interpreted the experimental results, and wrote the paper; N.-L.W., L.F., G.L., and J.L. contributed to the data analysis. All authors discussed the results and commented on the paper.

Additional information

Supplementary Information accompanies this paper at doi:10.1038/s41467-017-00446-2.

Competing interests: The authors declare no competing financial interests.

Reprints and permission information is available online at http://npg.nature.com/reprintsandpermissions/

Change History: A correction to this article has been published and is linked from the HTML version of this article.

Publisher's note: Springer Nature remains neutral with regard to jurisdictional claims in published maps and institutional affiliations.